A novel fully implicit finite volume method applied to the lid-driven cavity problem—Part I: High Reynolds number flow calculations

Mehmet Sahin and Robert G. Owens*,†

FSTI-ISE-LMF, Ecole Polytechnique Fédérale de Lausanne, CH 1015 Lausanne, Switzerland

SUMMARY

A novel implicit cell-vertex finite volume method is described for the solution of the Navier–Stokes equations at high Reynolds numbers. The key idea is the elimination of the pressure term from the momentum equation by multiplying the momentum equation with the unit normal vector to a control volume boundary and integrating thereafter around this boundary. The resulting equations are expressed solely in terms of the velocity components. Thus any difficulties with pressure or vorticity boundary conditions are circumvented and the number of primary variables that need to be determined equals the number of space dimensions. The method is applied to both the steady and unsteady two-dimensional lid-driven cavity problem at Reynolds numbers up to 10000. Results are compared with those in the literature and show excellent agreement. Copyright © 2003 John Wiley & Sons, Ltd.

KEY WORDS: implicit finite volume methods; lid-driven cavity flow; high Reynolds numbers; direct solver

1. INTRODUCTION

The lid-driven cavity flow of a Newtonian fluid has occupied the attention of the scientific computational community since the pioneering paper of Burggraf [1] back in 1966. Over the years the problem has spawned a huge number of papers; mainly concerned with the development of computational algorithms where, in a continuous drive to demonstrate the superior accuracy and stability properties of their latest numerical method, authors have applied it to one of the problem's two-dimensional rectangular or three-dimensional cubic forms.

Unsurprisingly, the majority of papers dealing with the numerical solution to the lid-driven cavity problem have been concerned with the two-dimensional problem, and accordingly and for the sake of brevity we will confine our literature review to computations in rectangles. In

---

* Correspondence to: R. G. Owens, FSTI-ISE-LMF, Ecole Polytechnique Fédérale de Lausanne, CH 1015 Lausanne, Switzerland.
† E-mail: robert.owens@epfl.ch

earlier papers the finite difference method was prominent and was adopted, for example, by Gatski *et al.* [2] (who used a velocity–vorticity formulation), Ghia *et al.* [3] in conjunction with a multigrid approach, Gustafson and Halasi [4, 5] who preferred the MAC method, and by Soh and Goodrich [6] and Goodrich *et al.* [7]. However, recent applications of finite difference schemes to the two-dimensional problem may sometimes be found in the literature: Kupferman [8], for example, used finite difference methods with a pure stream function formulation that bypassed the need for vorticity boundary conditions. More conventionally, Guo [9] used a staggered MAC-like second-order numerical scheme, applicable to either two or three-dimensional flows, for solving for flow in a two-dimensional square driven cavity at Reynolds numbers up to 3200. Papers for the two-dimensional problem incorporating finite element methods (see, for example References [10–12]), finite volume methods in various guises [13–15], boundary element methods [16–18], a radial basis function network method [19] and the lattice Boltzmann method [20], have also appeared in the recent literature.

The presence of corner singularities in both the two-dimensional and three-dimensional geometries is potentially hazardous for high-order methods of the spectral or *p*-finite element type, due to the Gibbs phenomenon. Particularly dangerous are the singularities at the points or lines of intersection between the moving lid and stationary walls since here the velocity field is discontinuous. Various high-order methods have been employed with success despite the difficulties associated with accuracy and control of oscillations near the corner/edge singularities, however. One manner in which these difficulties have been overcome is to change the problem: the tangential velocity on the moving lid is replaced by a polynomial that vanishes (together with at least its first derivatives) on the edges or corners where the lid and stationary walls meet. This is the so-called *regularized driven cavity problem*, assumed to have qualitatively the same dynamical properties as the driven cavity flow and solved to good effect by, for example, Shen [21], Leriche and Deville [22] and Botella [23]. A piecewise linear approximation to the constant tangential lid velocity, made to vanish at the lid-wall singularities was used by Barragy and Carey [24] in their *p*-finite element approach to the two-dimensional lid-driven problem. No modification was made to the original problem by Henderson [25] in his *hp*-adaptive spectral element method: his calculations sought to resolve the singularity directly through mesh refinement near the corners. Arguably, the most satisfactory solution to the lid-driven problem is to subtract off the leading part of the known asymptotic form of the Navier–Stokes singularity, leaving a more regular problem to be tackled, say, by a Chebyshev collocation method. This is what was done by Botella and Peyret [26, 27]. Of course, corner singularities between a stationary and a moving wall of the type described by the asymptotic expansions of Moffatt [28] and Botella and Peyret [27], amongst others, are physically unrealizable. The infinite acceleration of fluid particles implied by the change of boundary conditions requires an infinite stress at the corner. This observation was made by G.I. Taylor in 1962 in the context of the now famous 'scraper problem' [29]. What may be envisaged happening in reality for the lid-driven cavity problem is that fluid leaves or enters the cavity through 'leaks' along the lines of contact between the vertical walls and the moving lid. The unregularized lid-driven cavity problem is thus a mathematical idealization of the physical problem (and all the more so when one confines the flow to two dimensions!) However, Hansen and Kelmanson [30] have shown that as the leak heights tend to zero excellent agreement between the leaky and unregularized problems may be obtained. In the present paper we insert leaks across the heights of the finite volumes in the corners between the lid and the vertical walls for the two-dimensional problem. Although this regularizes the

problem somewhat, the leak heights are only 5.7656×10^{-5} for the finest mesh used in our computations in the unit square.

There are several difficulties with many of the approaches cited in the previous paragraphs. The primitive variable form of the Navier–Stokes equations is difficult to solve due to lack of an independent equation for the pressure term. Velocity–vorticity formulations of the Navier–Stokes equations have advantages over the velocity–pressure-based equations in that the pressure term is eliminated from the equations, and the well-known difficulty associated with wall pressure boundary conditions is avoided. However, a potential difficulty with this approach is that the vorticity value on the wall is not generally known a priori. Moreover, with the majority of three-dimensional velocity–vorticity methods it is necessary to solve three transport equations for the vorticity components and three Poisson equations (or their equivalents) for the velocity components [31]. For a discussion of the issue of vorticity boundary conditions, as well as a description of a new velocity–vorticity method requiring no vorticity boundary conditions and the determination of only N primary variables for N-dimensional problems ($N = 2, 3$), the reader is referred to Reference [31]. For earlier general reviews of the mathematical formulation of the incompressible Navier–Stokes equations we refer to References [32, 33] where a large number of references are mentioned.

The finite volume method proposed in this paper involves multiplication of the primitive variable-based momentum equation with the unit vector normal to a control volume boundary. Integration thereafter around the boundary of the same control volume thus eliminates the pressure term from the governing equations. Therefore any difficulty associated with the pressure term is avoided in a similar manner to that achieved by the velocity–vorticity formulation. Our method possesses two significant advantages over the majority of velocity–vorticity methods, however. First, unlike most velocity–vorticity formulations, no vorticity boundary conditions are required on the wall, since the resulting equations are expressed solely in terms of the velocity components. Only no-slip velocity boundary conditions are required. Secondly, the number of primary variables that need to be determined equals the number of space dimensions. The new velocity–vorticity formulation of Davies and Carpenter [31] referred to above also possesses these advantages over traditional velocity–vorticity methods. However, the method of Davies and Carpenter has been largely presented in the context of the disturbance equations in boundary layer flow and their method requires that the primary variables be constrained to satisfy certain limiting conditions. The method used in the present paper suffers from neither of these limitations and since the primary variables are just the components of velocity, no determination of secondary variables in an iterative or time-marching scheme is required. The implementation in this respect is thus straightforward.

In addition to requiring no vorticity or pressure boundary conditions and using only the velocity components as primary variables, our finite volume method is fully implicit. Implicit finite volume methods have enjoyed widespread use in the literature, due in part, no doubt, to their attractive stability properties and the utility of finite volume methods for problems defined in complex geometries. Confining our attention to just the past five years, for example, implicit finite volume methods have been employed to good effect for computing the evolution of surfactant concentration in investigations of the effects of surfactants on the rheological properties of emulsions [34] and on the shape of fluid interfaces in Stokes flow [35]. They have also been used in the simulation of three-dimensional mould filling problems in injection moulding [36]. Three-dimensional time-dependent viscoelastic flows have been tackled with implicit finite volume methods [37, 38], and they have seen service in the numerical modelling

of turbulence [39, 40]. Some attention in the literature has been given to the development and implementation of Krylov subspace methods for the resolution of the algebraic systems arising from a discretization using implicit finite volume methods of the convection–diffusion– reaction partial differential equations that describe the partially ionized flow in the boundary layer of a tokamak fusion reactor [40]. Comparisons have also been made of different Krylov subspace methods (GMRES, BiCGStab, etc.) for the solution of the algebraic systems of equations arising from an implicit finite volume approximation of the Navier–Stokes equations on unstructured grids [41]. For an analysis of cell-vertex finite volume methods for the cases of pure convection and convection–diffusion problems, the reader is referred to the papers of Morton and Stynes [42] and Morton *et al.* [43].

The present paper is organized as follows: in Section 2 we outline the governing equations and their discretization using our finite volume method. Both steady and time-dependent formulations of our method are described. In the steady form, a Newton method is employed. For both the steady and unsteady algorithms block Gaussian elimination is used for solving the resulting algebraic equations. Section 3 is dedicated to a discussion of the numerical results obtained for the two-dimensional lid-driven cavity problem at Reynolds numbers up to 10 000. Computations are performed on three meshes of increasing mesh density; with the finest of which are associated 132 098 degrees of freedom. The accuracy of the results at various Reynolds numbers in the literature for the two-dimensional driven cavity problem is usually assessed by performing a comparison of the streamwise and spanwise velocity profiles along the vertical and horizontal lines of symmetry with those of other authors, or by a quantitative comparison of the stream function value at the centre of the primary vortex, for example. Similar comparisons may be found in the present paper for the steady problem. Additionally, we consider convergence of the RMS value of the update vector for the velocity field in our Newton method, and demonstrate that this tends to zero in magnitude exponentially fast. Smooth solutions, in good (sometimes even excellent) agreement with those in the literature, are presented.

2. GOVERNING EQUATIONS AND NUMERICAL DISCRETIZATION

The incompressible unsteady Navier–Stokes equations may be written in dimensionless form over some domain $\Omega \subset \mathbb{R}^2$ as

$$\nabla \cdot \mathbf{u} = 0 \tag{1}$$

$$\frac{\partial \mathbf{u}}{\partial t} + (\mathbf{u} \cdot \nabla)\mathbf{u} = -\nabla p + \frac{1}{Re}\nabla^2 \mathbf{u} \tag{2}$$

where, in the usual notation, $\mathbf{u} = (u, v)$ denotes the velocity field, p the pressure and Re is a Reynolds number.

Suppose now that Ω may be partitioned into quadrilateral finite volumes $\Omega_{i,j}$ with (i, j) in some finite subset of $\mathbb{Z}^2$. Let $\mathbf{n}$ denote an outward pointing normal vector to the boundary $\partial\Omega_{i,j}$ of $\Omega_{i,j}$. Then integrating (1) over one such finite volume $\Omega_{i,j}$ we get, on application of the divergence theorem, that

$$\oint_{\partial\Omega_{i,j}} \mathbf{n} \cdot \mathbf{u} \, \mathrm{d}s = 0 \tag{3}$$
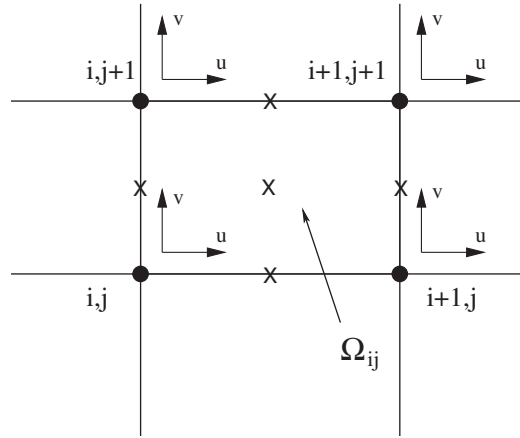
Figure 1. A four-node quadrilateral finite volume element Ω_{ij}.

Let us multiply (2) with $\mathbf{n}$ and integrate around the boundary $\partial\Omega_{i,j}$ of $\Omega_{i,j}$ to get

$$\oint_{\partial\Omega_{i,j}} \mathbf{n} \times \left[\frac{\partial\mathbf{u}}{\partial t} + (\mathbf{u}\cdot\nabla)\mathbf{u} + \nabla p - \frac{1}{Re}\nabla^2\mathbf{u}\right]\mathrm{d}s = \mathbf{0} \qquad (4)$$

Then (4) may be rewritten as

$$\oint_{\partial\Omega_{i,j}} \mathbf{n} \times \left[\frac{\partial\mathbf{u}}{\partial t} + (\nabla\times\mathbf{u})\times\mathbf{u} + \frac{1}{Re}\nabla\times(\nabla\times\mathbf{u})\right]\mathrm{d}s = \mathbf{0} \qquad (5)$$

Note that no pressure term appears in (3) and (5). In fact (5) is equal to the finite volume integral of the vorticity transport equation. However, here it is expressed solely in terms of the velocity components and therefore any difficulties associated with vorticity boundary conditions are obviated.

In this paper we will solve (3) and (5) for the velocity components in coupled form by using a direct solver. For the sake of simplicity (and only for this reason) our exposé shall be limited to rectangular control volumes with sides parallel to the Cartesian axes Ox and Oy, and $\Omega_{i,j}$ shall denote the cell having lower left-hand vertex labelled (i,j), as shown in Figure 1. The velocity unknowns $\mathbf{u}_{i,j}^n = (u_{i,j}^n, v_{i,j}^n)$ at the nth time step or Newton iterate are located at cell vertices and physical points are denoted $(x_{i,j}, y_{i,j})$ in an obvious way.

2.1. Time dependent Navier–Stokes equations

The continuity equation (3) is enforced at time level $t = (n+1)\Delta t$. To evaluate the integral over the boundary of $\Omega_{i,j}$, we use the mid-point rule on each of the four faces of $\Omega_{i,j}$, viz.

$$\oint_{\partial\Omega_{i,j}} \mathbf{n}\cdot\mathbf{u}^{n+1}\,\mathrm{d}s = \frac{v_{i+1,j+1}^{n+1} + v_{i,j+1}^{n+1}}{2}(x_{i+1,j+1} - x_{i,j+1}) - \frac{v_{i+1,j}^{n+1} + v_{i,j}^{n+1}}{2}(x_{i+1,j} - x_{i,j})$$

$$+ \frac{u_{i+1,j+1}^{n+1} + u_{i+1,j}^{n+1}}{2}(y_{i+1,j+1} - y_{i+1,j}) - \frac{u_{i,j+1}^{n+1} + u_{i,j}^{n+1}}{2}(y_{i,j+1} - y_{i,j}) \quad (6)$$

For the time-dependent problem we discretize the integrand in (5) with a Crank–Nicolson method which is second-order accurate in time:

$$\oint_{\partial\Omega_{i,j}} \mathbf{n} \times \left[\frac{\mathbf{u}^{n+1} - \mathbf{u}^n}{\Delta t} + \frac{\mathbf{E}^{n+1} + \mathbf{E}^n}{2} \right] \mathrm{d}s = 0 \quad (7)$$

where $\mathbf{E}^n$ in (7) is defined by

$$\mathbf{E}^n = (E_1^n, E_2^n) = \omega^n \times \mathbf{u}^n + \frac{1}{Re}\nabla\times\omega^n \quad (8)$$

The line integral in (7) is evaluated using the mid-point rule on each of the cell faces, this yielding

$$\frac{(y_{i+1,j+1} - y_{i+1,j})}{2} \left[\frac{(v_{i+1,j+1}^{n+1} - v_{i+1,j+1}^n)}{\Delta t} + \frac{(v_{i+1,j}^{n+1} - v_{i+1,j}^n)}{\Delta t} + E_{2,i+1,j+1/2}^{n+1} + E_{2,i+1,j+1/2}^n \right]$$

$$- \frac{(x_{i+1,j+1} - x_{i,j+1})}{2} \left[\frac{(u_{i+1,j+1}^{n+1} - u_{i+1,j+1}^n)}{\Delta t} + \frac{(u_{i,j+1}^{n+1} - u_{i,j+1}^n)}{\Delta t} + E_{1,i+1/2,j+1}^{n+1} + E_{1,i+1/2,j+1}^n \right]$$

$$- \frac{(y_{i,j+1} - y_{i,j})}{2} \left[\frac{(v_{i,j+1}^{n+1} - v_{i,j+1}^n)}{\Delta t} + \frac{(v_{i,j}^{n+1} - v_{i,j}^n)}{\Delta t} + E_{2,i,j+1/2}^{n+1} + E_{2,i,j+1/2}^n \right]$$

$$+ \frac{(x_{i+1,j} - x_{i,j})}{2} \left[\frac{(u_{i+1,j}^{n+1} - u_{i+1,j}^n)}{\Delta t} + \frac{(u_{i,j}^{n+1} - u_{i,j}^n)}{\Delta t} + E_{1,i+1/2,j}^{n+1} + E_{1,i+1/2,j}^n \right] = 0 \quad (9)$$

The flux vector components $E_{1,i+1/2,j}$ and $E_{2,i,j+1/2}$ appearing in (9) are computed as follows:

$$E_{1,i+1/2,j} = -\tfrac{1}{4}(v_{i,j} + v_{i+1,j})(\omega_{i+1/2,j+1/2} + \omega_{i+1/2,j-1/2})$$

$$+ \frac{1}{Re} \frac{\omega_{i+1/2,j+1/2} - \omega_{i+1/2,j-1/2}}{y_{i+1/2,j+1/2} - y_{i+1/2,j-1/2}} \quad (10)$$

$$E_{2,i,j+1/2} = \tfrac{1}{4}(u_{i,j} + u_{i,j+1})(\omega_{i+1/2,j+1/2} + \omega_{i-1/2,j+1/2})$$

$$- \frac{1}{Re} \frac{\omega_{i+1/2,j+1/2} - \omega_{i-1/2,j+1/2}}{x_{i+1/2,j+1/2} - x_{i-1/2,j+1/2}} \quad (11)$$

The non-linearities in $E_{1,i+1/2,j}^{n+1}$ and $E_{2,i,j+1/2}^{n+1}$ are treated by taking the velocity components (u,v) from the previous time step. To handle the vorticity terms in (10) and (11) a vorticity

value at the centre of the (i, j)th cell $\Omega_{i,j}$ is calculated as

$$\omega_{i+1/2, j+1/2} = \frac{1}{\text{Area } \Omega_{i,j}} \oint_{\partial \Omega_{i,j}} \mathbf{n} \times \mathbf{u} \, \mathrm{d}s \qquad (12)$$

where the line integral on the right-hand side of (12) is evaluated using the mid-point rule on each of the cell faces, as before.

2.2. Steady Navier–Stokes equations

The same finite volumes described in Section 2.1 are used in the discretization of the steady problem. Let a superscript n now denote an iteration count. The steady form of (3) and (5) is solved using Newton's method: substituting $\mathbf{u} = \mathbf{u}^{n+1}$ into (3) and (5) where

$$\mathbf{u}^{n+1} = \mathbf{u}^n + \delta \mathbf{u}^{n+1} \qquad (13)$$

and neglecting second-order terms we get

$$\oint_{\partial \Omega_{i,j}} \mathbf{n} \cdot \delta \mathbf{u}^{n+1} \, \mathrm{d}s = - \oint_{\partial \Omega_{i,j}} \mathbf{n} \cdot \mathbf{u}^n \, \mathrm{d}s \qquad (14)$$

and

$$\oint_{\partial \Omega_{i,j}} \mathbf{n} \times \left[\delta \omega^{n+1} \times \mathbf{u}^n + \omega^n \times \delta \mathbf{u}^{n+1} + \frac{1}{Re} \nabla \times \delta \omega^{n+1} \right] \mathrm{d}s = - \oint_{\partial \Omega_{i,j}} \mathbf{n} \times \mathbf{E}^n \, \mathrm{d}s \qquad (15)$$

(14) and (15) are discretized in a similar manner to Equations (6) and (7) and solved in coupled form using a direct solver. The new values of the velocity components at the $(n+1)$th iteration are calculated as follows:

$$\mathbf{u}_{i,j}^{n+1} = \mathbf{u}_{i,j}^n + \delta \mathbf{u}_{i,j}^{n+1} / \beta \qquad (16)$$

where β is an under-relaxation parameter chosen in order to ensure convergence. In the present calculations its value is set equal to 5.0.

For both the steady and unsteady algorithms described in the previous two sections, mass conservation (Equations (6) and (14)) is applied in each finite volume. The vorticity transport equation (Equations (7) and (15)) is applied in each finite volume except those next to the walls, vorticity creation thus being permitted within these latter elements in order to satisfy the no-slip boundary conditions. The resulting algebraic systems of equations for the cell vertex values of $\mathbf{u}^{n+1}$ or $\delta \mathbf{u}^{n+1}$ are block quad-diagonal and are solved at each step (time step or Newton iterate) by using block Gaussian elimination. Considerable computational time has been saved with extensive use of the Intel Math Kernel Library for block matrix–matrix and matrix–vector operations.

3. NUMERICAL RESULTS

In order to verify its accuracy at high Reynolds numbers and compute the base flow required for a linear stability analysis (see Part II of this paper [44]), the present fully implicit velocity formulation is applied to steady lid-driven cavity flow in a square $[0, 1] \times [0, 1]$, as shown in
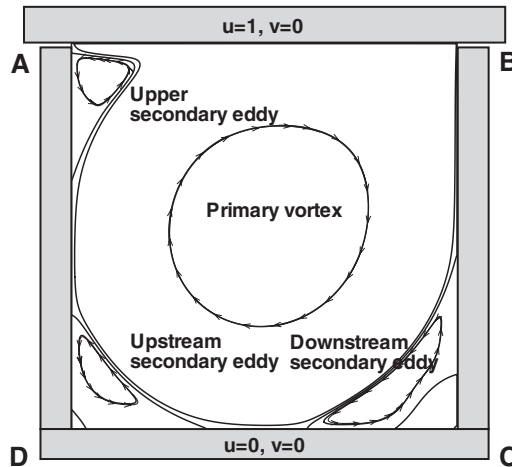
Figure 2. Lid-driven cavity boundary conditions with the basic features of cavity flow.

Figure 2. The singularities situated between the lid and the cavity walls (at points *A* and *B* of Figure 2), are handled by introducing 'leaks' over the height of the upper corner finite volumes. In fact, this is the most suitable way of applying the physical boundary conditions. The mass flow between the lid and the cavity wall weakens the primary vortex strength within the cavity, depending on the size of the leaks. As the size of these leaks approaches zero, however, the solutions converge towards the solutions obtained with the physically unrealizable boundary conditions [30].

In the present work three different grids are employed: coarse (M1: 129×129 grid points), medium (M2: 193×193 grid points) and fine (M3: 257×257 grid points), in order to investigate grid dependency of the solution. These are shown in Figure 3. The smallest finite volume cells are those situated at corners A and B and have heights 1.1665×10^{-4}, 7.7170×10^{-5} and 5.7656×10^{-5} for the coarse, medium and fine grids, respectively. As mentioned above, these cell sizes correspond to the size of the leaks between the lid and the vertical cavity walls. As may be seen in Figure 3, the highest density of grid points is to be found near the lid and walls. This is done in order to make the size of the leaks as small as possible and to resolve adequately the very thin boundary layers on the lid and cavity walls.

The first numerical results correspond to the solution of the steady Navier–Stokes equations on the finest grid (M3) at Reynolds numbers ranging from 0 to 10 000 where the Reynolds number for this flow is based on the lid velocity and cavity height. For the solution of the steady Navier–Stokes equations, Newton's method is used, as explained in Section 2.2. The initial conditions for Newton's method are calculated from the direct solution of Stokes flow. Then the flow at $Re = 100$, 400, 1000, 3200, 5000, 7500 and 10 000 is solved using the previous solution as an initial condition.

The computed streamlines are presented in Figure 4. At $Re = 0$, the streamlines and vorticity contours are symmetric about the vertical centreline of the cavity. At the lower corners upstream and downstream secondary eddies are visible and are equal in size. Although the analytical solution predicts an infinite number of exponentially decaying eddies at the
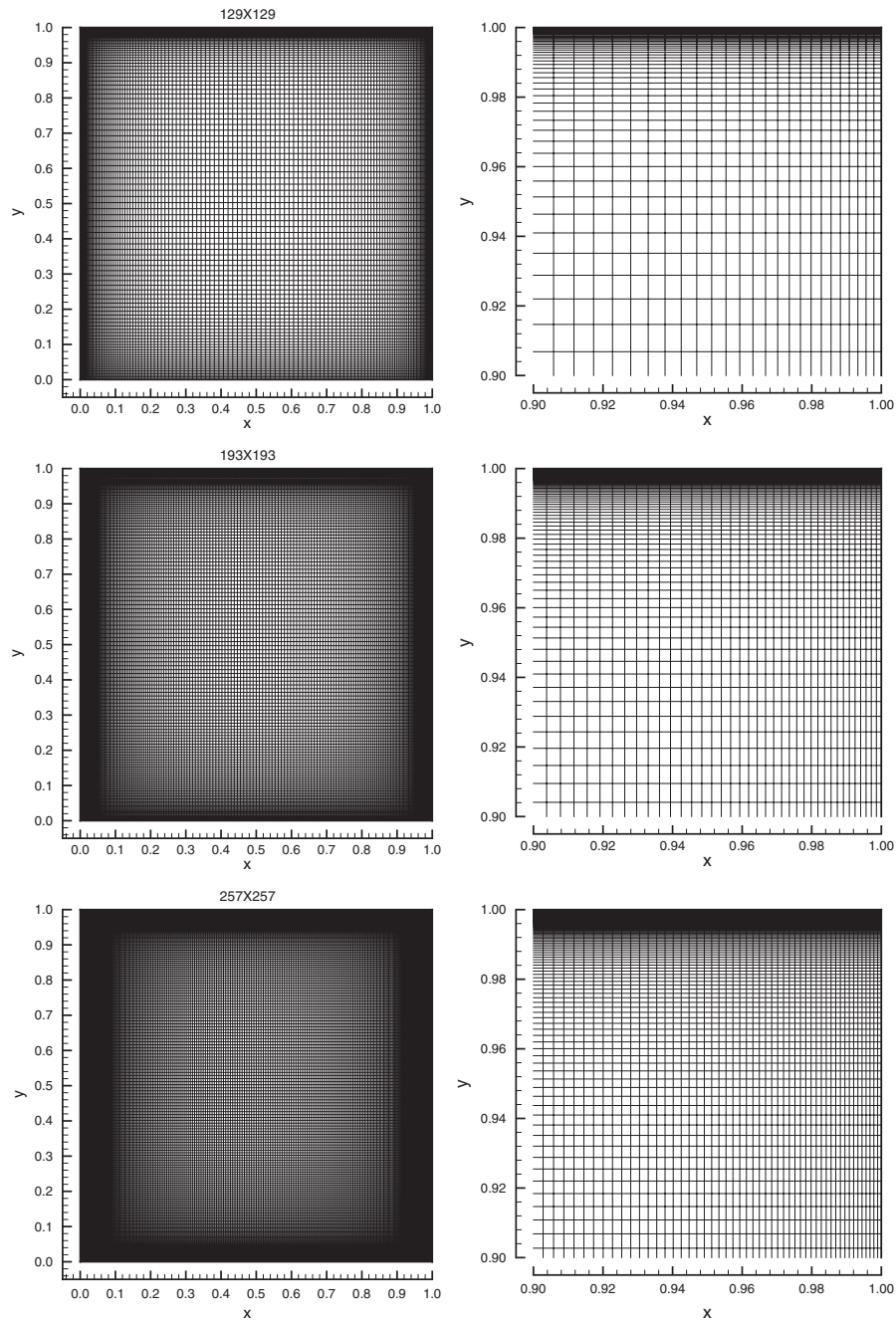
Figure 3. The three computational meshes (with detail of the top right-hand corner) used for the calculations presented in this paper. Top to bottom: Mesh M1 (129×129 grid points), Mesh M2 (193×193 grid points), Mesh M3 (257×257 grid points).
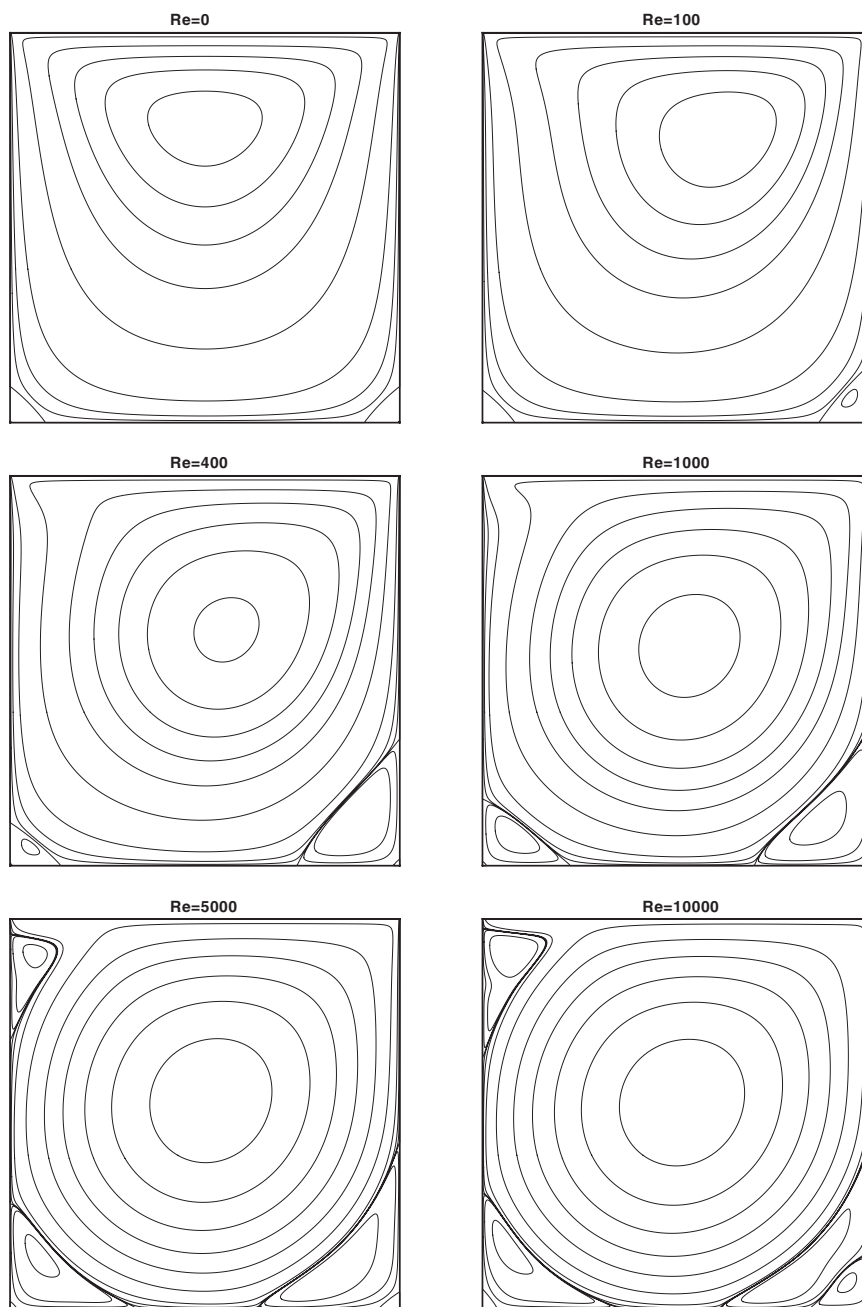
Figure 4. Streamlines computed with mesh M3. Reynolds numbers from 0 to 10 000. The stream function equals 0 on the cavity boundary and the contour levels shown for each plot are -0.11, -0.09, -0.07, -0.05, -0.03, -0.01, -0.001, -0.0001, -0.00001, 0.0, 0.00001, 0.0001, 0.001 and 0.01.

Re=0
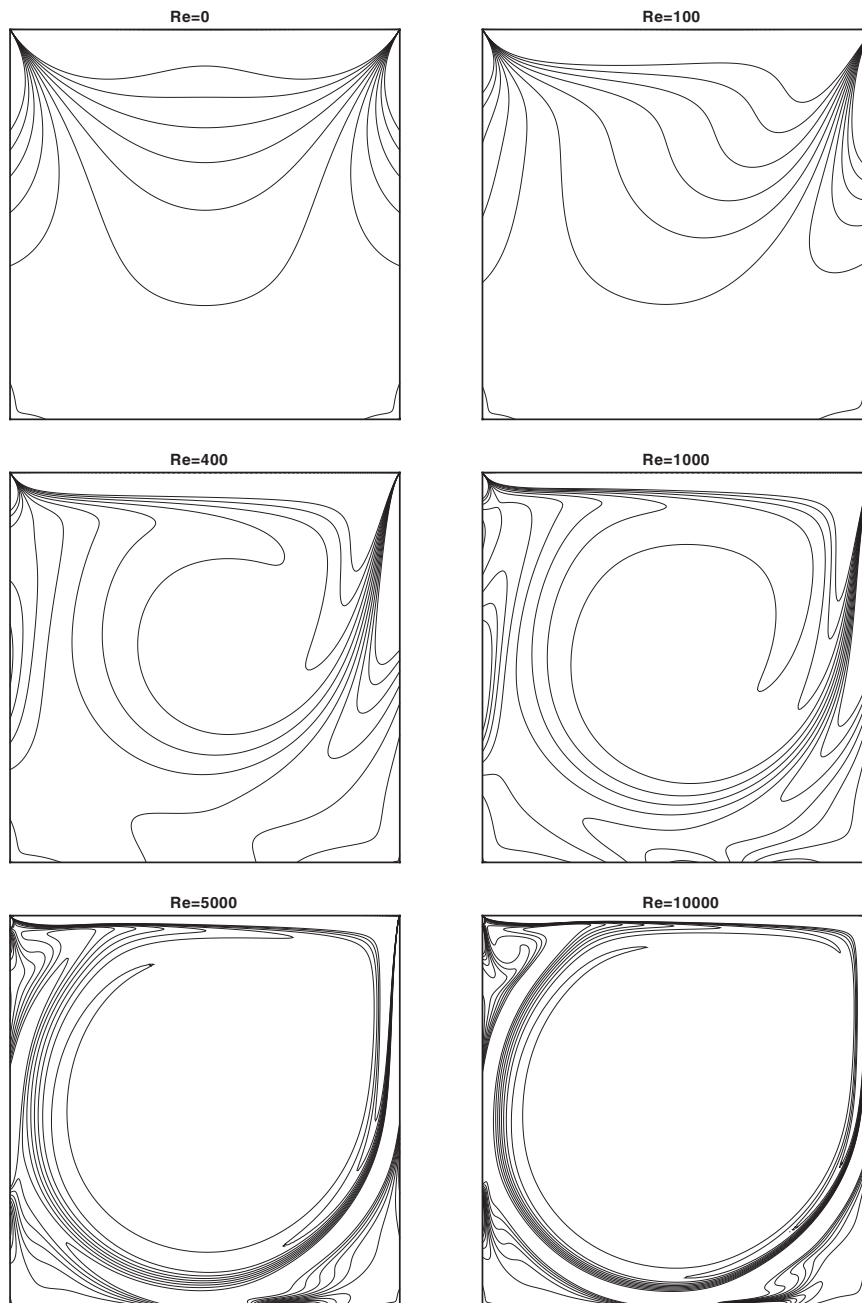
Re=100

Re=400

Re=1000

Re=5000

Re=10000

Figure 5. Contours of vorticity computed with mesh M3. Reynolds numbers from 0 to 10 000. Contour levels shown for each plot are -5.0, -4.0, -3.0, -2.0, -1.0, 0.0, 1.0, 2.0, 3.0, 4.0 and 5.0.

Table I. Table of vorticity values at the primary vortex centre. Mesh M3.

Re	Vorticity at primary vortex centre
0	−3.2208
100	−3.1655
400	−2.2950
1000	−2.0664
3200	−1.9593
5000	−1.9392
7500	−1.9275
10 000	−1.9231

corners [28], it is not possible to resolve these eddies with a finite number of grid points. At a Reynolds number of around 100, the primary vortex moves towards the right-hand wall and the downstream secondary eddy starts to enlarge in size. At a Reynolds number of 400, the primary vortex starts to move towards the cavity centre and it continues to move to the centre even at high Reynolds numbers. Evidence of growth in the upstream secondary eddy at a Reynolds number of 400 is also now visible. If the Reynolds number is increased further another secondary eddy emerges on the upper left-hand cavity wall. Further increases in the Reynolds number makes visible tertiary level vortices. It might be considered surprising that smooth solutions at these high Reynolds numbers are possible with a central difference scheme. However, Hafez and Soliman [45], who also used a central difference scheme, presented solutions of the steady Navier–Stokes equations for the lid-driven cavity problem at Reynolds numbers up to 30 000 obtained using a Newton method combined with a direct solver.

In Figure 5 we note that as the Reynolds number increases the vorticity contours move away from the cavity centre towards the cavity walls and indicates that very strong vorticity gradients develop on the lid and the cavity walls (especially the right-hand vertical wall) for higher Reynolds numbers. In contrast, in the centre of the cavity almost no vorticity gradient is evident at all. The fluid begins to rotate like a rigid body with a constant angular velocity. The vorticity values at the centre of the primary vortex—as computed with mesh M3—are shown in Table I. As the Reynolds number increases there is a clear trend towards the theoretical infinite Re value of −1.886 (see Burggraf [1]).

For an assessment of the accuracy of the present results, the velocity components through the vertical and horizontal centrelines of the cavity are compared with the corresponding numerical results of Ghia et al. [3] in Figures 6 and 7. The comparison shows good agreement, particularly at Reynolds numbers up to 5000. However, at a Reynolds number of 10 000 the present method (featuring a non-uniform grid) gives slightly higher extremal values of the velocity components since it is difficult to resolve the very thin boundary layer with a uniform grid, even with one as fine as the 257×257 grid of Ghia et al. [3]. As may be seen from Figures. 6 and 7, as the Reynolds number increases the extremal values of the velocity components increase in magnitude and the turning points get progressively closer to the wall. The values of the extrema in the velocity components and the minimum values of the stream function are given in Table II and are compared with other results in the literature. Although the results at low Reynolds numbers are in good agreement, at high Reynolds number they deviate from each other, particularly at $Re = 10\,000$. The present results are in

Figure 6. Profiles of u along the line $x = 0.5$ computed with mesh M3. Reynolds numbers from 0 to 10 000. Also shown are the results ($\square$) of Ghia *et al*. [3].

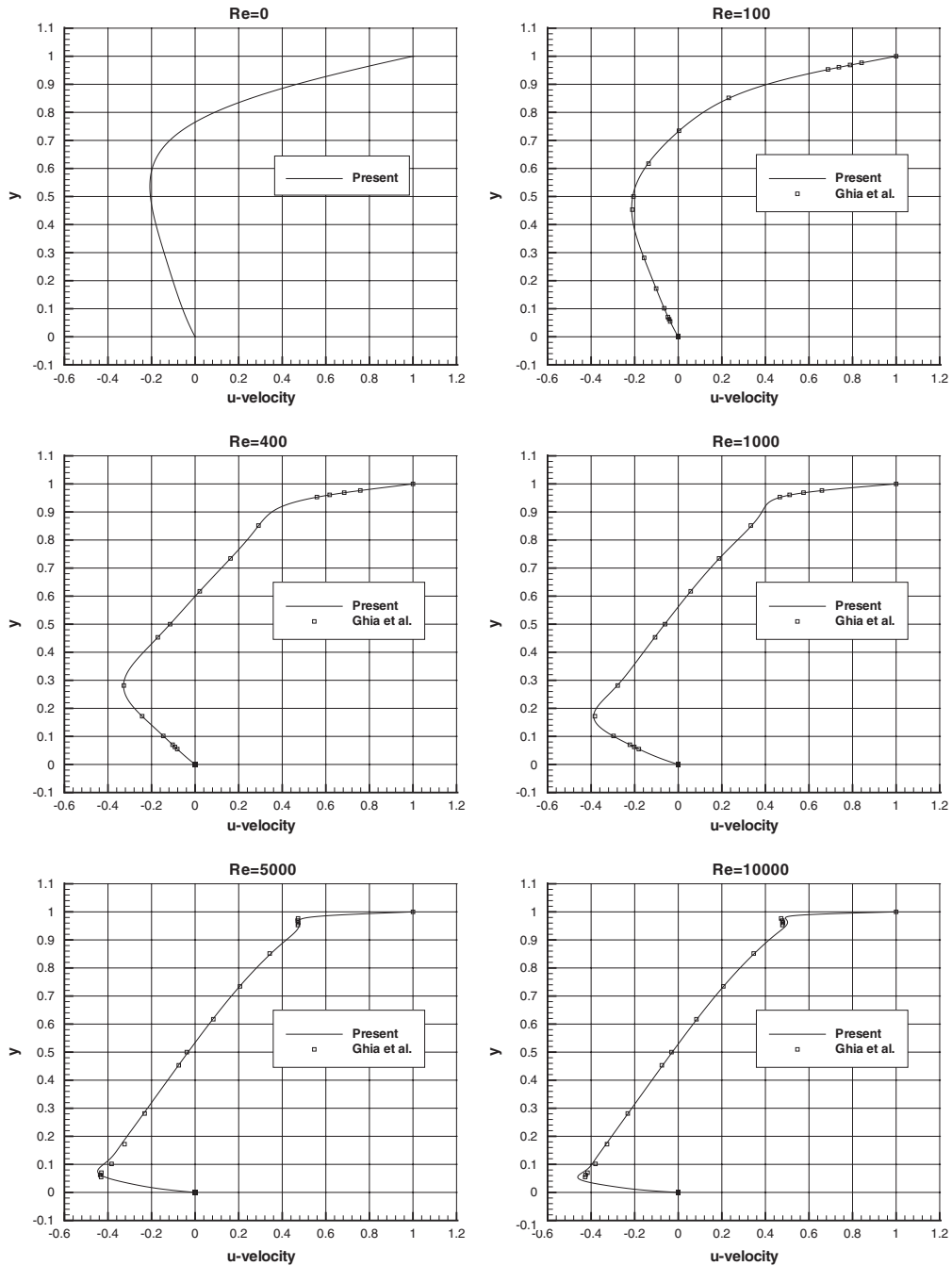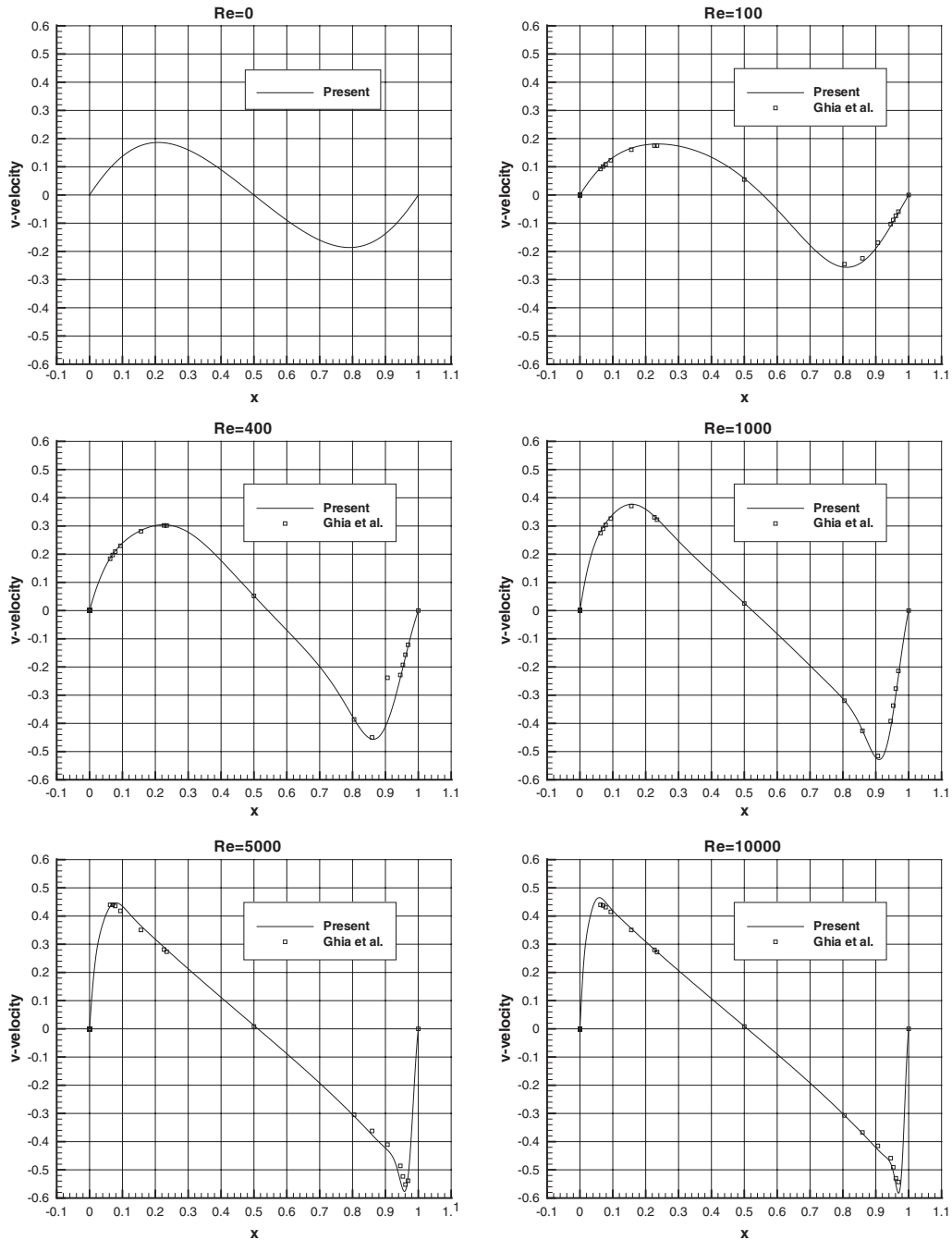Figure 7. Profiles of v along the line $y = 0.5$ computed with mesh M3. Reynolds numbers from 0 to 10 000. Also shown are the results ($\square$) of Ghia *et al.* [3].

Table II. Table of (a) minimum values of u computed along $x = 0.5$ and the corresponding ordinate y_{min}, (b) maximum values of v computed along $y = 0.5$ and the corresponding abscissa x_{max}, (c) minimum values of v computed along $y = 0.5$ and the corresponding abscissa x_{min} and the corresponding abscissa x_{min}, (d) minimum values of ψ and the corresponding coordinates x_{min}, y_{min}.

Reference	u_{min}	y_{min}	v_{max}	x_{max}	v_{min}	x_{min}	ψ_{min}	x_{min}, y_{min}
$Re = 0$								
Present	−0.207754	0.5376	0.186273	0.2105	−0.186273	0.7894	−0.100054	0.5000,0.7626
Botella and Peyret [26]	—	—	—	—	—	—	−0.100076	—
$Re = 100$								
Present	−0.213924	0.4598	0.180888	0.2354	−0.256603	0.8127	−0.103471	0.6189,0.7400
Ghia et al. [3]	−0.21090	0.4531	0.17527	0.2344	−0.24533	0.8047	−0.103423	0.5172,0.7344
Botella and Peyret [26]	−0.214042	0.4581	0.179572	0.2370	−0.253803	0.8104	—	—
Hou et al. [20]	—	—	—	—	—	—	−0.1030	0.6196,0.7373
Bruneau and Jouron [46]	−0.2106	0.4531	0.1786	0.2344	−0.2521	0.8125	−0.1026	0.6172,0.7344
Deng et al. [47]	−0.21315	—	0.17896	—	−0.25339	—	—	—
$Re = 400$								
Present	−0.328375	0.2815	0.304447	0.2253	−0.456316	0.8621	−0.113897	0.5536,0.6075
Ghia et al. [3]	−0.32726	0.2813	0.30203	0.2266	−0.44993	0.8594	−0.113909	0.5547,0.6055
Hou et al. [20]	—	—	—	—	—	—	−0.1121	0.5608,0.6078
Deng et al. [47]	−0.32751	—	0.30271	—	−0.45274	—	—	—
$Re = 1000$								
Present	−0.388103	0.1727	0.376910	0.1573	−0.528447	0.9087	−0.118800	0.5335,0.5639
Ghia et al. [3]	−0.38289	0.1719	0.37095	0.1563	−0.51550	0.9063	−0.117929	0.5313,0.5625
Botella and Peyret [26]	−0.388569	0.1717	0.376944	0.1578	−0.527077	0.9092	−0.118936	0.5308,0.5652
Barragy and Carey [24]	—	—	—	—	—	—	−0.118930	—
Hou et al. [20]	−0.3764	0.1602	0.3665	0.1523	−0.5208	0.9102	−0.1178	0.5333,0.5647
Bruneau and Jouron [46]	−0.38511	—	0.37369	—	−0.52280	—	−0.1163	0.5313,0.5586
$Re = 3200$								
Present	−0.435402	0.0921	0.432448	0.0972	−0.569145	0.9491	−0.121628	0.5201,0.5376
Ghia et al. [3]	−0.41933	0.1016	0.42768	0.0938	−0.54053	0.9453	−0.120377	0.5165,0.5469
$Re = 5000$								
Present	−0.447309	0.0741	0.446913	0.0799	−0.576652	0.9573	−0.122050	0.5134,0.5376
Ghia et al. [3]	−0.43643	0.0703	0.43648	0.0781	−0.55408	0.9531	−0.118966	0.5117,0.5352
Barragy and Carey [24]	—	—	—	—	—	—	−0.122219	0.5151,0.5359
Hou et al. [20]	—	—	—	—	—	—	−0.1214	0.5176,0.5373
Bruneau and Jouron [46]	−0.4359	0.0664	0.4259	0.0762	−0.5675	0.9590	−0.1142	0.5156,0.5313
$Re = 7500$								
Present	−0.456054	0.0610	0.458048	0.0670	−0.580994	0.9649	−0.122302	0.5134,0.5289
Ghia et al. [3]	−0.43590	0.0625	0.44030	0.0703	−0.55216	0.9609	−0.119976	0.5117,0.5322
Barragy and Carey [24]	—	—	—	—	—	—	−0.122380	0.5132,0.5321
Hou et al. [20]	—	—	—	—	—	—	−0.1217	0.5176,0.5333
Bruneau and Jouron [46]	−0.4379	0.0508	0.4179	0.0625	−0.5640	0.9688	−0.1113	0.5156,0.5234
$Re = 10000$								
Present	−0.461617	0.0549	0.465210	0.0598	−0.582351	0.9684	−0.122489	0.5134,0.5289
Ghia et al. [3]	−0.42735	0.0547	0.43983	0.0625	−0.54302	0.9688	−0.119731	0.5117,0.5333
Barragy and Carey [24]	—	—	—	—	—	—	−0.122393	0.5113,0.5302
Bruneau and Jouron [46]	−0.4373	0.0430	0.4141	0.0547	−0.5610	0.9727	−0.1053	0.5156,0.5234

Table III. Variation in location of the secondary eddies with Re number. Mesh M3.

Re	Downstream secondary eddy		Upstream secondary eddy		Upper secondary eddy	
	x_{max}, y_{max}	ψ_{max}	x_{max}, y_{max}	ψ_{max}	x_{max}, y_{max}	ψ_{max}
0	0.9630,0.0378	0.222065E-05	0.0369,0.0378	0.222065E-05	—	—
100	0.9424,0.0610	0.126584E-04	0.0332,0.0352	0.179303E-05	—	—
400	0.8835,0.1203	0.640440E-03	0.0508,0.0461	0.142720E-04	—	—
1000	0.8658,0.1119	0.172397E-02	0.0826,0.0776	0.233014E-03	—	—
3200	0.8259,0.0847	0.282335E-02	0.0799,0.1203	0.111207E-02	0.0530,0.8984	0.705801E-03
5000	0.8081,0.0741	0.306508E-02	0.0720,0.1382	0.136890E-02	0.0621,0.9108	0.143828E-02
7500	0.7894,0.0642	0.322261E-02	0.0645,0.1525	0.151998E-02	0.0670,0.9108	0.211980E-02
10 000	0.7796,0.0610	0.319479E-02	0.0598,0.1624	0.159044E-02	0.0694,0.9108	0.261144E-02

very close agreement with those of Barragy and Carey [24] and the maximum difference in the minimum value of the stream function computed by these authors and by us is less than 0.138%. The results of Botella and Peyret [26], calculated with a Chebyshev collocation method and featuring subtraction of the leading part of the corner singularities, are believed to be very accurate but their results do not extend to high Reynolds numbers. In addition, in Table III we present results showing how the location of the secondary eddies change with the Reynolds number.

In order to demonstrate the convergence characteristics of the present method, we calculate the RMS value RMS(n) of the update vector $\delta\mathbf{u}^{n+1}$ at the $(n+1)$th Newton iterate as

$$\text{RMS}(n) = \sqrt{\frac{1}{N_x N_y} \sum_{i,j=1}^{N_x,N_y} (u_{i,j}^{n+1} - u_{i,j}^n)^2 + (v_{i,j}^{n+1} - v_{i,j}^n)^2} = \frac{1}{\beta\sqrt{N_x N_y}} \|\delta\mathbf{u}^{n+1}\|_2 \qquad (17)$$

where N_x and N_y denote the number of grid points in the x and y directions, respectively. Figure 8 shows a plot on a log-normal scale of RMS(n) versus the iteration number n at Reynolds numbers of 100 and 10 000. The figure shows an exponential decay in RMS(n) and in both cases RMS(n) is of the order of 1×10^{-8} after 70 Newton iterations. From our numerical experiments it would seem that the rate of convergence is independent of the Reynolds number for a sufficiently large value of β. To gain insight into why this might be so, we follow an approximate error analysis and consider the non-linear system (3) and (5) summed up over the appropriate i, j and supplemented with velocity boundary conditions. This system might be written in the form

$$\mathbf{F}(\mathbf{u}) = \mathbf{0} \qquad (18)$$

for some vector-valued functional $\mathbf{F}$, so that from (16)

$$\mathbf{u}^{n+1} - \mathbf{u}^n = -\frac{1}{\beta} \left(\frac{\partial \mathbf{F}}{\partial \mathbf{u}}\right)_{\mathbf{u}=\mathbf{u}^n}^{-1} \mathbf{F}(\mathbf{u}^n) \qquad (19)$$

and

$$\mathbf{u}^{n+2} - \mathbf{u}^{n+1} = -\frac{1}{\beta} \left(\frac{\partial \mathbf{F}}{\partial \mathbf{u}}\right)^{-1}_{\mathbf{u}=\mathbf{u}^{n+1}} \mathbf{F}(\mathbf{u}^{n+1}) \tag{20}$$

We let ε_n denote the L_2 norm of $\mathbf{u}^{n+1} - \mathbf{u}^n$ and from (19)–(20) see that

$$\frac{\varepsilon_{n+1}}{\varepsilon_n} = \frac{\|(\partial \mathbf{F}/\partial \mathbf{u})^{-1}_{\mathbf{u}=\mathbf{u}^{n+1}} \mathbf{F}(\mathbf{u}^{n+1})\|_2}{\|(\partial \mathbf{F}/\partial \mathbf{u})^{-1}_{\mathbf{u}=\mathbf{u}^n} \mathbf{F}(\mathbf{u}^n)\|_2}$$

$$\approx \frac{\|(\partial \mathbf{F}/\partial \mathbf{u})^{-1}_{\mathbf{u}=\mathbf{u}^{n+1}}[\mathbf{F}(\mathbf{u}^n) - 1/\beta(\partial \mathbf{F}/\partial \mathbf{u})_{\mathbf{u}=\mathbf{u}^n}(\partial \mathbf{F}/\partial \mathbf{u})^{-1}_{\mathbf{u}=\mathbf{u}^n} \mathbf{F}(\mathbf{u}^n)]\|_2}{\|(\partial \mathbf{F}/\partial \mathbf{u})^{-1}_{\mathbf{u}=\mathbf{u}^n} \mathbf{F}(\mathbf{u}^n)\|_2}$$

$$= \left(1 - \frac{1}{\beta}\right) \frac{\|(\partial \mathbf{F}/\partial \mathbf{u})^{-1}_{\mathbf{u}=\mathbf{u}^{n+1}} \mathbf{F}(\mathbf{u}^n)\|_2}{\|(\partial \mathbf{F}/\partial \mathbf{u})^{-1}_{\mathbf{u}=\mathbf{u}^n} \mathbf{F}(\mathbf{u}^n)\|_2} \tag{21}$$

Supposing that the Jacobian matrix is approximately constant, Equation (21) leads to

$$\frac{\varepsilon_{n+1}}{\varepsilon_n} \approx 1 - \frac{1}{\beta} \tag{22}$$

so that

$$\log \varepsilon_{n+1} - \log \varepsilon_n = \log \left(1 - \frac{1}{\beta}\right) \tag{23}$$

and hence

$$\log \varepsilon_n - \log \varepsilon_0 = n \log \left(1 - \frac{1}{\beta}\right) \tag{24}$$

From the above relation we computed the gradient of the function $\varepsilon_n/\sqrt{N_x N_y}$ of n and found this to be -0.0969 for $\beta = 5.0$. This is identical to four decimal places with the slopes computed from the RMS plots for $Re = 100$ and $10\,000$ shown in Figure 8. However this level of agreement may not hold at even higher Reynolds numbers since it may not be possible to use the same β value in order to maintain convergence. The initial value of the RMS depends upon the difference between the initial condition and the converged solution. This explains why the initial RMS value and all subsequent RMS values at $Re = 100$ are larger than those computed at the same iteration count at $Re = 10\,000$.

The second set of numerical results corresponds to the time-dependent direct numerical simulation of an impulsively accelerated lid-driven cavity flow at a Reynolds number of $10\,000$. The streamlines of the time-dependent solutions at this Reynolds number are presented in Figure 9 at non-dimensional time levels of 2.00, 4.00, 6.00, 8.00, 10.00 and 12.00. The formation of the primary vortex and its transport towards the cavity centre may be seen clearly. On the current PC (with a 1200 MHz Pentium IV processor) we could only afford to continue calculations up to a non-dimensional time level of 20.00, although we would like to determine at which Reynolds number a Hopf bifurcation takes place by computing
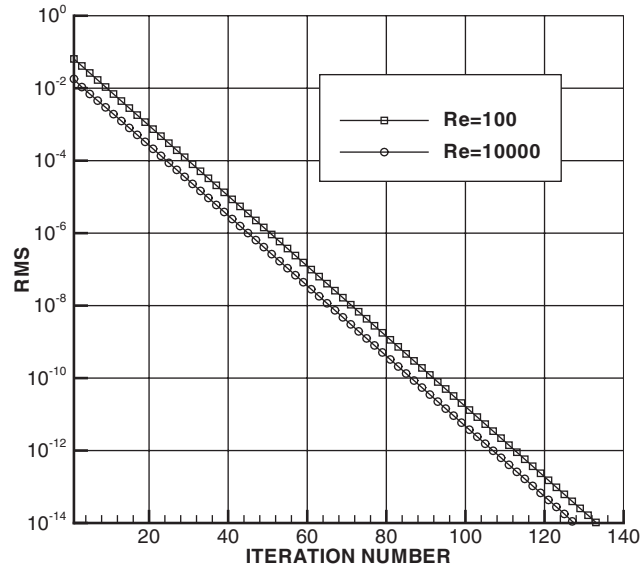
Figure 8. RMS value RMS(n) (see Equation (17)) against iteration number n. Mesh M3. $\beta = 5.0$.

time-accurate solutions. Unfortunately, near the critical Reynolds number the most dangerous eigenvalue has a real part which is very small. As a consequence, determination of whether or not a steady solution exists at a near-critical Reynolds number may take a very long time and is computationally very expensive. Therefore, in Part II of this paper [44] we employ a linear stability analysis to determine the critical Reynolds number at which a Hopf bifurcation takes place.

4. CONCLUSIONS

A novel finite volume method has been presented for the solution of both the steady and unsteady incompressible Navier–Stokes equations. The method involves multiplication of the primitive-variable based momentum equation with a unit vector normal to a finite volume boundary and subsequent integration of this equation along the boundary of the same control volume. Thus any difficulties associated with the pressure term or vorticity boundary conditions are obviated. The velocity components are solved in strong coupled form by using a direct solver. The method is applied to the lid-driven cavity problem for both steady and unsteady flows at Reynolds numbers up to 10 000. Our solutions are smooth and in excellent agreement with benchmark results in the literature. Use of a direct solution technique ensures a solenoidal velocity field at each iterative or time step for the steady and unsteady cases, respectively.

Although we have presented only a two-dimensional application of the present method, the extension of the method to three-dimensional problems would be interesting since there are only three unknowns that would need to be determined, which is lower than both the primitive-variable based and most velocity–vorticity formulations [31]. This may be done by imposing the continuity equation within each control volume and by computing the closed-line
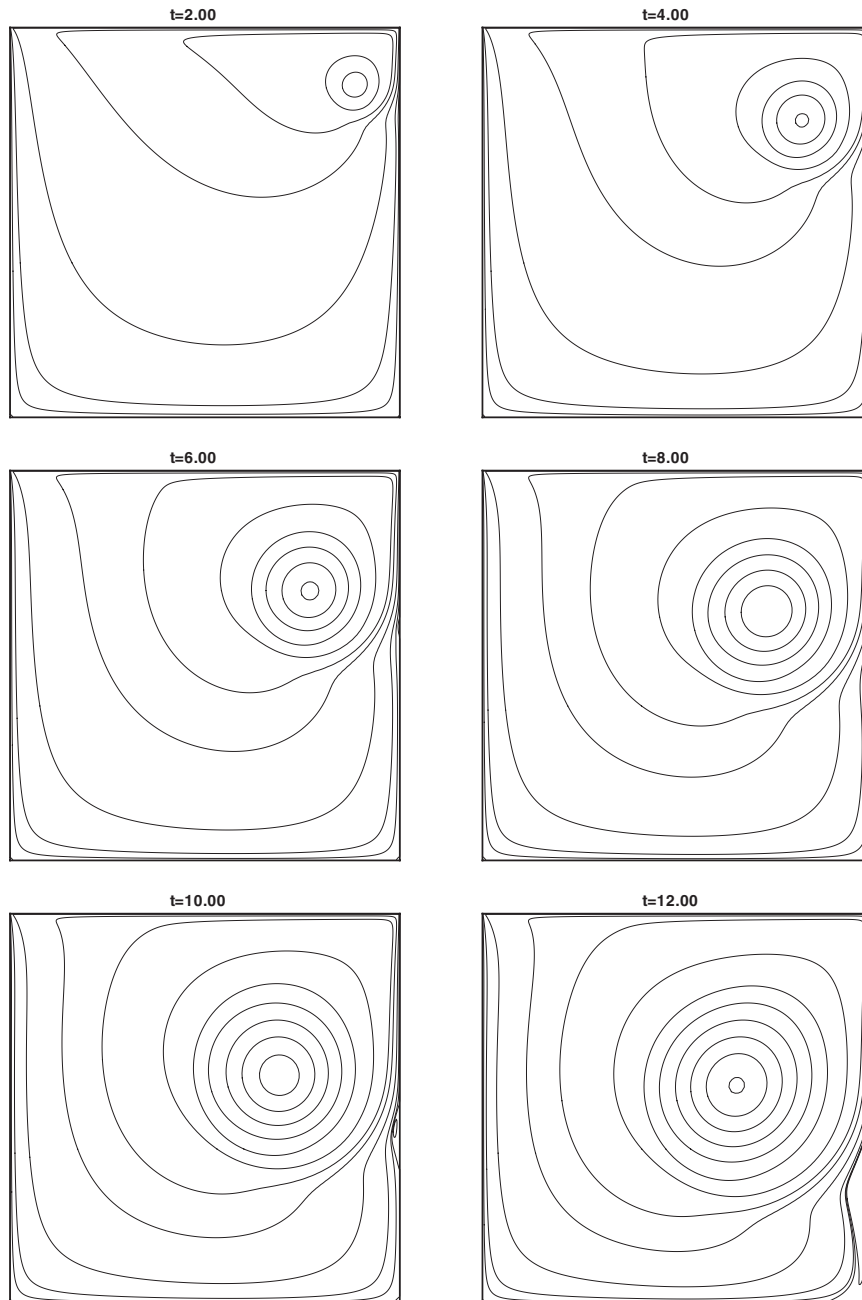
Figure 9. Contours of computed streamlines with mesh M2 for an impulsively accelerated lid-driven cavity at $Re = 10\,000$. Contour levels shown for each plot are -0.10, -0.09, -0.08, -0.07, -0.06, -0.05, -0.04, -0.03, -0.02, -0.01, -0.005, -0.001, -0.0001, -0.00001, 0.0, 0.00001, 0.0001, 0.001 and 0.005.

integral of the product of a normal vector with the momentum equation around the control volume faces in a similar manner to (5). A weakness of the present method, however, is that due to the linear dependence of some of the closed-line integrals, it may be difficult to match the number of equations to the number of unknowns for more complex configurations. One possible solution, for cuboidal finite volumes, at least, might be to adopt a staggered grid arrangement with velocity components now defined at the centre of the faces with respect to which they point in the normal direction.

REFERENCES

1. Burggraf OR. Analytical and numerical studies of the structure of steady separated flows. *Journal of Fluid Mechanics* 1966; **24**(1):113–151.
2. Gatski TB, Grosch CE, Rose ME. A numerical study of the two-dimensional Navier–Stokes equations in vorticity–velocity variables. *Journal of Computational Physics* 1982; **48**(1):1–22.
3. Ghia U, Ghia KN, Shin CT. High-Re solutions for incompressible flow using the Navier–Stokes equations and a multigrid method. *Journal of Computational Physics* 1982; **48**(3):387–411.
4. Gustafson K, Halasi K. Vortex dynamics of cavity flows. *Journal of Computational Physics* 1986; **64**(2): 279–319.
5. Gustafson K, Halasi K. Cavity flow dynamics at higher Reynolds number and higher aspect ratio. *Journal of Computational Physics* 1987; **70**(2):271–283.
6. Soh WY, Goodrich JW. Unsteady solution of incompressible Navier–Stokes equations. *Journal of Computational Physics* 1988; **79**(1):113–134.
7. Goodrich JW, Gustafson K, Halasi K. Hopf bifurcation in the driven cavity. *Journal of Computational Physics* 1990; **90**(1):219–261.
8. Kupferman R. A central-difference scheme for a pure stream function formulation of incompressible viscous flow. *SIAM Journal on Scientific Computing* 2001; **23**(1):1–18.
9. Guo DX. A second order scheme for the Navier–Stokes equations: application to the driven-cavity problem. *Applied Numerical Mathematics* 2000; **35**(4):307–322.
10. Allievi A, Bermejo R. Finite element modified method of characteristics for the Navier–Stokes equations. *International Journal for Numerical Methods in Fluids* 2000; **32**(4):439–464.
11. Kjellgren P. A semi-implicit fractional step finite element method for viscous incompressible flows. *Computational Mechanics* 1997; **20**:541–550.
12. Liu CH, Leung DYC. Development of a finite element solution for the unsteady Navier–Stokes equations using projection method and fractional-θ-scheme. *Computer Methods in Applied Mechanics and Engineering* 2001; **190**(32–33):4301–4317.
13. Calhoon WH, Roach RL. A naturally upwinded conservative procedure for the incompressible Navier–Stokes equations on non-staggered grids. *Computers & Fluids* 1997; **26**(5):525–545.
14. Chang S, Haworth DC. Adaptive grid refinement using cell-level and global imbalances. *International Journal for Numerical Methods in Fluids* 1997; **24**(4):375–392.
15. Wright NG, Gaskell PH. An efficient multigrid approach to solving highly recirculating flows. *Computers & Fluids* 1995; **24**(1):63–79.
16. Aydin M, Fenner RT. Boundary element analysis of driven cavity flow for low and moderate Reynolds numbers. *International Journal for Numerical Methods in Fluids* 2001; **37**(1):45–64.
17. Grigoriev MM, Fafurin AV. A boundary element method for steady viscous fluid flow using penalty function formulation. *International Journal for Numerical Methods in Fluids* 1997; **25**(8):907–929.
18. Grigoriev MM, Dargush GF. A poly-region boundary element method for incompressible viscous fluid flows. *International Journal for Numerical Methods in Engineering* 1999; **46**(7):1127–1158.
19. Mai-Duy N, Tran-Cong T. Numerical solution of Navier–Stokes equations using multiquadric radial basis function networks. *International Journal for Numerical Methods in Fluids* 2001; **37**(1):65–86.
20. Hou S, Zou Q, Chen S, Doolen G, Cogley AC. Simulation of cavity flow by the lattice Boltzmann method. *Journal of Computational Physics* 1995; **118**(2):329–347.

21. Shen J. Hopf bifurcation of the unsteady regularized driven cavity flow. *Journal of Computational Physics* 1991; **95**(1):228–245.
22. Leriche E, Deville MO. A Uzawa-type pressure solver for the Lanczos-τ-Chebyshev spectral method. *Computers & Fluids* 2003; submitted.
23. Botella O. On the solution of the Navier–Stokes equations using Chebyshev projection schemes with third-order accuracy in time. *Computers & Fluids* 1997; **26**(2):107–116.
24. Barragy E, Carey GF. Stream function-vorticity driven cavity solution using *p* finite elements. *Computers & Fluids* 1997; **26**(5):453–468.
25. Henderson RD. Dynamic refinement algorithms for spectral element methods. *Computer Methods in Applied Mechanics and Engineering* 1999; **175**(3–4):395–411.
26. Botella O, Peyret R. Benchmark spectral results on the lid-driven cavity flow. *Computers & Fluids* 1998; **27**(4):421–433.
27. Botella O, Peyret R. Computing singular solutions of the Navier–Stokes equations with the Chebyshev-collocation method. *International Journal for Numerical Methods in Fluids* 2001; **36**(2):125–163.
28. Moffatt HK. Viscous and resistive eddies near a sharp corner. *Journal of Fluid Mechanics* 1964; **18**(1):1–18.
29. Taylor GI. On scraping viscous fluid from a plane surface. In *Miszellaneen der Angewandten Mechanik* (*Fetschrift Walter Tollmein*), Schäfer M (ed.). Akademie-Verlag: Berlin, 1962; 313–315.
30. Hansen EB, Kelmanson MA. An integral equation justification of the boundary conditions of the driven cavity problem. *Computers & Fluids* 1994; **23**(1):225–240.
31. Davies C, Carpenter PW. A novel velocity–vorticity formulation of the Navier–Stokes equations with applications to boundary layer disturbance evolution. *Journal of Computational Physics* 2001; **172**(1): 119–165.
32. Gatski TB. Review of incompressible fluid flow computations using the vorticity–velocity formulation. *Applied Numerical Mathematics* 1991; **7**(3):227–239.
33. Gresho PM. Incompressible fluid dynamics: Some fundamental formulation issues. *Annual Review of Fluid Mechanics* 1991; **23**:413–453.
34. Pozrikidis C. Numerical investigation of the effect of surfactants on the stability and rheology of emulsions and foam. *Journal of Engineering Mathematics* 2001; **41**(2–3):237–258.
35. Pozrikidis C. Numerical studies of cusp formation at fluid interfaces in Stokes flow. *Journal of Fluid Mechanics* 1998; **357**:29–57.
36. Chang RY, Yang WH. Numerical simulation of mold filling in injection molding using a three-dimensional finite volume approach. *International Journal for Numerical Methods in Fluids* 2001; **37**(2):125–148.
37. Xue SC, Phan-Thien N, Tanner RI. Fully three-dimensional, time-dependent numerical simulations of Newtonian and viscoelastic flows in a confined cylinder—Part I. Method and steady flows. *Journal of Non-Newtonian Fluid Mechanics* 1999; **87**(2–3):337–367.
38. Xue SC, Tanner RI, Phan-Thien N. Three-dimensional numerical simulations of viscoelastic flows—predictability and accuracy. *Computers Methods in Applied Mechanics and Engineering* 1999; **180**(3–4): 305–331.
39. Meister A, Oevermann M. An implicit finite volume approach of the k-ε turbulence model on unstructured grids. *Zeitschrift Fur Angewandte Mathematik und Mechanik* 1998; **78**(11):743–757.
40. Sedaghat A, Ackroyd JAD, Wood NJ. Turbulence modelling for supercritical flows including examples with passive shock control. *Aeronautical Journal* 1999; **103**(1020):113–125.
41. Meister A. Comparison of different Krylov subspace methods embedded in an implicit finite volume scheme for the computation of viscous and inviscid flow fields on unstructured grids. *Journal of Computational Physics* 1998; **140**(2):311–345.
42. Morton KW, Stynes M. An analysis of the cell vertex method. *RAIRO—Modél. Math. Anal. Numér.* 1994; **28**(6):699–724.
43. Morton KW, Stynes M, Suli E. Analysis of a cell-vertex finite volume method for convection–diffusion problems. *Mathematics of Computation* 1997; **66**(220):1389–1406.
44. Sahin M, Owens RG. A novel fully-implicit finite volume method applied to the lid-driven cavity problem. Part II. Linear stability analysis. *International Journal for Numerical Methods in Fluids* 2003; **42**:79–88.
45. Hafez M, Soliman M. Numerical solution of the incompressible Navier–Stokes equations in primitive variables on unstaggered grids. In *Incompressible Computational Fluid Dynamics,* Gunzberger MD, Nicolaides RA (eds). Cambridge University Press: Cambridge, 1993; 183–201.
46. Bruneau C-H, Jouron C. An efficient scheme for solving steady incompressible Navier–Stokes equations. *Journal of Computational Physics* 1990; **89**(2):389–413.
47. Deng GB, Piquet J, Queutey P, Visonneau M. Incompressible-flow calculations with a consistent physical interpolation finite-volume approach. *Computers & Fluids* 1994; **23**(8):1029–1047.
48. Knoll DA, McHugh PR. Enhanced nonlinear iterative techniques applied to a nonequilibrium plasma flow. *SIAM Journal on Scientific Computing* 1998; **19**(1):291–301.